CHEMISTRY OF MATERIALS

pubs.acs.org/cm

Article

Synthesis of Micron-Sized WS_2 Crystallites Using Atomic Layer Deposition and Sulfur Annealing

Kamesh Mullapudi, Rafik Addou, Charles. L. Dezelah, Daniel F. Moser, Ravindra K. Kanjolia, Jacob H. Woodruff, and John. F. Conley, Jr.*

Cite This: *Chem. Mater.* 2023, 35, 4649−4659

Read Online

ACCESS | Metrics & More | Article Recommendations | Supporting Information

ABSTRACT: The synthesis of micron-sized WS_2 crystallites via atomic layer deposition (ALD) is reported for the first time using bis(*t*-butylimido)bis-(trimethylsilylmethyl)tungsten and H_2S as reactants, followed by post-deposition annealing. Self-limiting growth on silicon is demonstrated between 315 and 350 °C. As-deposited films are nanocrystalline, comprising a mix of WS_2 and WO_3 phases along with residual amounts of WO_xN_y and SiO_x impurities. Post-deposition annealing in elemental sulfur at 600 °C induces the emergence of the 2LA(M), $E_{2g}^1(\Gamma)$, and $A_{1g}(\Gamma)$ Raman vibration modes for WS_2 and increases crystallite size up to a few microns, the largest reported to date for ALD WS_2. The growth substrate was found to impact WS_2 morphology. Films grown and annealed on silicon produced two distinct morphologies of WS_2 crystallites with (i) in-plane multilayered flake pyramids predominantly seen at 650 °C and (ii) out-of-plane "flowers" growing at 700 and 800 °C. Films grown and annealed on ZnS showed only out-of-plane "crumpled" flowers with a high density of WS_2 edge sites suitable for catalysis, while films grown and annealed on Al_2O_3 showed predominately few-layered in-plane WS_2 flakes, suitable for electronic devices.

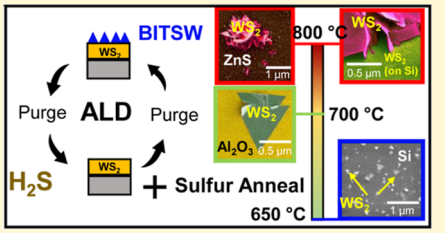

1. INTRODUCTION

Transition metal dichalcogenides (TMDs) such as MoS_2 and WS_2 have garnered interest due to their potential application in hydrogen evolution reaction (HER) catalysis,[1−5] tribology,[6,7] energy storage,[8−10] and optoelectronics.[11] In addition to their high theoretical mobility, the presence of a finite, tunable band gap makes TMDs an attractive alternative to graphene or silicon sheets for next-generation field effect transistors (FETs).[12−21] All of these applications require films with high crystallinity and morphologies ranging from high edge-site density 3D structures to two-dimensional (2D) monolayers. Due to its higher theoretical mobility, WS_2 is even more attractive than MoS_2 for FET applications.[14]

Methods of WS_2 synthesis include mechanical exfoliation,[15] chemical vapor deposition,[22−24] hydrothermal deposition,[25] solution-based deposition,[2] sulfurization of WO_3 films,[16,25,27] and epitaxy.[17] Although these methods have been reported to achieve crystallite sizes and morphologies suitable for the above applications, they face challenges in terms of scalability, uniformity, conformality, and/or high processing temperatures. Atomic layer deposition (ALD) is a layer-by-layer deposition technique based on purge-separated self-limiting surface reactions that are capable of depositing uniform films with high conformality over large substrates and 3D structures with high aspect ratios. The added benefits of lower process temperatures than CVD and layer-by-layer thickness control make it an attractive technique to synthesize WS_2. In the first half of a typical ALD cycle, a precursor is pulsed into the reactor, where it is allowed to chemisorb or react with the substrate until saturation. This is followed by an inert gas purge, which removes the excess reactant/byproduct(s) from the reactor. In the second half of the ALD cycle, the co-reactant is pulsed and allowed to react with the surface until saturation and, ideally, complete the formation of a monolayer of the film. Another inert gas purge once again removes the excess co-reactant and its byproducts from the reactor. The entire cycle is repeated, with the film depositing one layer at a time, until the desired thickness is reached.

A summary of reported WS_2 crystallite sizes for ALD processes is shown in Figure 1. In the first report of ALD WS_2, Scharf et al. used WF_6 and H_2S as precursors, assisted by an added pulse of diethylzinc every few ALD cycles to promote nucleation and growth.[6,7] A temperature range of 300−350 °C was investigated, but saturation was not reported. While films deposited at 300 °C showed little crystallinity, *ex situ* annealing in vacuum at 500 °C yielded 30 nm sized grains, which were analyzed using SEM.[6] A higher deposition temperature of 350 °C showed a slight improvement in crystallite size to 40−70 nm for out-of-plane (0 0 2) and to 50−100 nm for in-plane (1 0 0) and (1 0 1) peaks, with the latter peaks only seen at 350 °C.[7]

Received: January 2, 2023
Revised: May 24, 2023
Published: June 9, 2023

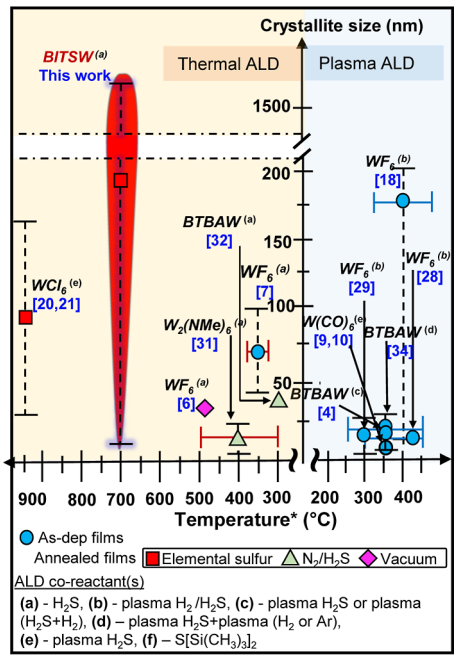

Figure 1. Summary of crystallite sizes for thermal and plasma-enhanced ALD WS_2 films as-deposited and annealed under various environments.

Delabie et al. demonstrated the use of a sacrificial Si seed layer and H_2 plasma as reducing agents to enable the WF_6/H_2S process.[28] Whereas no deposition occurred between 250 and 450 °C on ALD Al_2O_3, the addition of a sacrificial Si layer allowed pulsed CVD of 2D WS_2 layers at 450 °C. By inserting an H_2 plasma step in between the WF_6 and H_2S, they were able to achieve PEALD of WS_2 at 300 °C on ALD Al_2O_3. As-deposited PEALD WS_2 was polycrystalline with a domain size of 5−10 nm (measured using TEM). A temperature-dependent orientation of WS_2 crystallites was observed, similar to that of Scharf et al.[7] They later investigated the addition of the H_2 plasma pulse, finding that shorter H_2 plasma times resulted in little WS_2 growth, while longer exposure times yielded sulfur-deficient films with S/W ratios in the range of 0.6−1.8. WS_2 crystal domains of up to 20 nm, with (002) basal planes parallel to the substrate, were seen via high-resolution electron microscopy (HREM) for films deposited at 300 °C with an increase in mosaicity seen at 450 °C.[29] For a fixed H_2 plasma exposure time, they reported growth saturation on ALD Al_2O_3 at 300 °C. However, the process did not appear to saturate with H_2 plasma exposure time. In a subsequent study using the same precursors, they investigated the influence of the substrate, processing temperatures, and reactor pressure to control diffusion kinetics during PEALD WS_2 film growth and improve the crystallite size. A lower reactivity of WF_6 on SiO_2, when coupled with a higher processing temperature and reactor pressure (8 Torr), yielded crystallites up to 200 nm in size.[18] WS_2 crystallite sizes of up to 160 nm were grown employing the same precursors in a PEALD process at 450 °C by using pre-patterned WS_2 seed layers.[30]

To address issues with the nucleation of WF_6 on various substrates, other halide precursors have been explored. Browning et al. used alternating cycles of WCl_5 and H_2S to deposit WS_2 on SnS at 390 °C to form WS_2/SnS heterojunctions but did not report saturating growth.[19] More recently, Yang et al. used cycles of WCl_6 and bis(trimethylsilyl)sulfide $[S(Si(CH_3)_3)_2]$ at 400 °C to deposit WS_2 on sapphire. As-deposited films were sulfur rich (S/W = 2.3). In-plane lateral growth was found to dominate for thicknesses up to 5.6 nm, while out-of-plane vertical growth was seen for films thicker than 20 nm. Following annealing at 950 °C in sulfur, films were crystallized into planar WS_2 flakes (with a maximum diameter of 108 nm) and vertical nanowires.[20] Using similar process parameters, the same group later reported a maximum WS_2 grain size of 160 nm.[21]

Four metal−organic tungsten precursors have been investigated in previous studies. ALD using $W(CO)_6$ and H_2S was first investigated by Nandi et al., who observed a constant growth rate of amorphous WS_2 films over a temperature window of 175−205 °C with precursor decomposition above 205 °C.[8] Saturation of the $W(CO)_6$ pulse was shown at an unspecified temperature. Later studies using $W(CO)_6$ with plasma H_2S reported PEALD of out-of-plane WS_2 nanoflakes up to 10 nm in size at 350 °C.[9,10]

Kim et al. reported thermal ALD using tris(hexyne)-tungstenmonocarbonyl $[W(CO)(C_6H_{10})_3]$ and H_2S to deposit WS_2 over a temperature range of 200−300 °C. As-deposited films were amorphous and sulfur-deficient (S/W = 0.43). Post-deposition annealing in H_2S above 700 °C improved film crystallinity and S/W to 1.46.[3] Mattinen et al. reported the use of $W_2(NMe)_6$ and H_2S to deposit WS_2 over a temperature window of 130−200 °C. As-deposited films were amorphous and sulfur deficient with an S/W ratio of 0.87. A mild post-deposition *in situ* anneal in H_2S at 400 °C improved S/W to 1.82 and yielded crystallites up to 10 nm in size with a considerable disorder.[31] Finally, the widely used metal−organic precursor bis(*t*-butylimido)bis(dimethylamido)-tungsten [BTBAW] was first investigated by Wu et al. to deposit WS_2 using H_2S at 300 °C, which yielded WS_2 nanoplatelets 30 nm in diameter on carbon nanotube substrates.[32] BTBAW has also been used with $(t\text{-}C_4H_9)_2S_2$ to deposit crystalline WS_2 at 400 °C on SiO_2/Si and at 350 °C on Au substrates.[33] Balasubramanyam et al. later reported the use of BTBAW with either H_2S plasma or a plasma mixture of H_2S + H_2 to tailor the properties of synthesized crystallites. Films deposited at 300 °C using H_2S plasma were found to yield a sulfur-rich film (S/W = 2.2) comprising densely packed WS_2 nanoflakes ranging in size from 10 to 20 nm. However, a mixed H_2S + H_2 plasma produced sulfur-deficient (S/W = 1.8) 3D tapered fin structures.[4] More recently, Balasubramanyam et al. developed an ABC or atomic layer annealing (ALA)-type ALD process that included an extra Ar + H_2 plasma exposure in each cycle (BTBAW/Ar purge/H_2S plasma/Ar purge/Ar + H_2 plasma). The extra Ar + H_2 plasma step suppressed WS_2 vertical nanostructure growth for films deposited at 300 °C but resulted in sulfur-deficient films (S/W ∼ 1.7). WS_2 average grain sizes of 19 and 24 nm were found with and without the Ar + H_2 plasma step, respectively.[34]

Experimental mobility of WS_2 is limited by the crystallite flake size through carrier scattering at grain boundaries. Despite all the efforts described, there have been no reports of synthesis of WS_2 crystallites larger than one micron using ALD. In this work, we report a new thermal ALD process for WS_2 using bis(*t*-butylimido)bis(trimethylsilylmethyl)tungsten [hereafter referred to as BITSW][35] and H_2S. The BITSW precursor is an advanced variant of the BTBAW precursor used in ref 32. The new BITSW compound replaces the dimethylamido ligands with trimethylsilylmethyl ligands for additional stability and higher reactivity toward sulfur-

https://doi.org/10.1021/acs.chemmater.3c00013
Chem. Mater. 2023, 35, 4649−4659

containing ligands and both dimethylamido and trimethylsilylmethyl ligands are expected to react with sulfur-containing co-reactants. Film deposition was investigated over a temperature range of 200−365 °C. Although single monolayer thickness control was not achieved, self-limiting growth was observed between 315 and 350 °C. The composition by chemical state and stoichiometry of as-deposited films were measured using X-ray photoelectron spectroscopy (XPS). X-ray diffraction (XRD) showed that as-deposited films were nanocrystalline and that post-deposition annealing at 600 °C and above in elemental sulfur improved crystallinity, with Raman spectroscopy revealing characteristic modes of WS_2. Scanning electron microscopy (SEM) showed crystallites larger than 1 μm, the largest reported for an ALD-based process to date, with morphology and size dependent upon the substrate and annealing temperature.

2. EXPERIMENTAL METHODS

ALD was performed in a modified Arradiance GEMStar 2010 cross-flow reactor using a heteroleptic tungsten source, W-(tBuN)$_2$(CH$_2$SiMe$_3$)$_2$ (abbreviated as BITSW), and a 3.5% H_2S in N_2 gas mixture as the co-reactant.[36] BITSW is stable up to at least 328 °C. Additional details on the physical properties of BITSW are available in our previous work. (For convenience, Figure S1 shows a thermo-gravimetric analysis plot of percent weight loss vs temperature and a power-compensated differential scanning calorimetry scan of heat flow vs temperature, along with a drawing of the BITSW structure taken from Mullapudi et al.).[35] BITSW was heated to 110 °C in a 150 mL NSI stainless-steel vapor-drawn ampoule to generate sufficient vapor pressure (see Figure S1c). The hot walls of the Gemstar reaction chamber were maintained at 300 °C, while the substrates were heated separately using a 6 inch diameter stainless-steel heater fabricated at Belilove Company-Engineers, CA. The substrate temperature, T_{DEP}, was calibrated against the higher set-point temperature of the substrate heater using a SensArray process probe wafer. The delivery lines connecting the precursor ampoules to the reaction chamber were held at 180 °C to maintain a sufficient thermal gradient and prevent precursor condensation. A continuous N_2 flow was maintained, with a 40 sccm flow used as a carrier gas to deliver (pulse) reactants to the chamber and a 120 sccm flow used to purge the chamber. An additional precursor "*soak*" step, which involved closing off the reaction chamber to the exhaust pump, was inserted in between each *pulse* and *purge* sequence. A 5 s soak and 90 s purge were found to be optimum in achieving the best film uniformity over a 5 inch wafer area. Therefore, a pulse sequence of 1:5:90:0.2:5:90 s [BITSW/soak/N_2 purge/H_2S/soak/N_2 purge] was used throughout this study, unless mentioned otherwise. The reaction chamber was maintained at ∼0.8 Torr throughout the process.

Films were deposited on three different types of 1 inch × 1 inch coupons: (i) ∼1.5 nm native SiO_2/Si, (ii) 30 nm of ALD Al_2O_3/Si, and (iii) 4.5 nm of ZnS/Si. Si substrate orientation was (1 0 0). ZnS was deposited separately via ALD in the same reactor using 50 cycles of diethylzinc (DEZ) and H_2S at 250 °C. Al_2O_3 films were deposited in a Picosun SUNALE R-150 thermal ALD reactor using 300 cycles of trimethylaluminum (TMA) and H_2O at 150 °C.

Ex situ elemental sulfur anneals were performed in an Applied Test Systems 2 inch diameter single-zone quartz furnace at atmospheric pressure. A detailed schematic illustration of the setup is shown in the Supporting Information (Figure S2). A continuous 100 sccm N_2 flow (Industrial Welding Supply CAS: 7727-37-9) was used as the carrier gas and maintained in the furnace throughout the anneal. First, to remove any residual moisture, the quartz tube was flushed with the N_2 flow for 1.5 h while being held at 100 °C. WS_2 films deposited on various substrates were then introduced into the furnace using a silicon carrier wafer. A ceramic crucible containing about ∼500 mg of 99.5% sulfur powder (Acros Organics CAS: 7704-34-9) was placed upstream of the hot zone at an appropriate distance to maintain it at 180−200 °C, at which the vapor pressure is approximately 1 Torr. The temperature of the crucible was measured using a thermocouple and was sufficient to melt and generate sulfur vapor required for the anneal. A fixed 70 min of ramp up time was used for all anneals, following which annealing was performed for 60 min. Subsequently, the tube was then allowed to cool to 100 °C, while maintaining the continuous N_2 flow. To trap excess vaporized sulfur and prevent back-streaming of moisture and O_2 during each anneal, a mineral oil bubbler was fitted to the exhaust.

Spectroscopic ellipsometry (SE) was performed on as-deposited films using a J. A. Woollam M2000 ellipsometer over a wavelength range of 1.25−4.90 eV and modeled using CompleteEASE software. A Cauchy layer on top of a 1.5 nm SiO_2/Si substrate was first used to model the thickness and refractive index at 1.96 eV (632.8 nm), where ultrathin WS_2 may be assumed to be sufficiently transparent.[37] A spline layer was fit using the extracted thickness and refractive index. Two Tauc-Lorentz (TL) oscillators were then used to parameterize this layer in order to model optical absorption at photon energies greater than 2.0 eV and to ensure Kramers-Kronig consistency (see Figure S3). Grazing-incidence XRD measurements were performed using a Rigaku Ultima IV XRD diffractometer equipped with a Cu Kα source. Scans were acquired at a grazing incidence angle of 0.9° in a parallel beam geometry. Following each isochronal anneal and a subsequent GIXRD measurement, a small portion of the analyzed sample (∼1 cm × 1 cm) was diced and stored in an inert gas (Ar) container. Scanning electron microscopy (SEM) images of these stored samples were then acquired within the next 48 h using FEI Quanta 3D. An electron acceleration voltage of 5 keV and a probe current of 100 nA were used to image the observed crystallites. Energy-dispersive X-ray (EDX) analysis was performed using the same instrument at a higher electron acceleration voltage of 20 keV. Crystallite size distribution was analyzed using a watershed thresholding algorithm in Gwyddion software. Backscattered Raman spectra were acquired using a HORIBA LabRAM Raman spectrometer equipped with an unpolarized 532 nm laser source. A 100× objective was used to align and focus the laser beam onto the surface of the sample. Laser power was maintained at 1 mW using an attenuation filter prior to incidence in order to avoid laser-induced damage or crystallization.[38] Raman spectra were then acquired using a grating resolution of 1800 gratings/mm. Acquired peaks were fitted with pseudo-Voigt line shapes (40:60, Gaussian/Lorentzian) using Fityk software. Optical microscopy was performed using an Axiotron optical micrograph. X-ray photoelectron spectroscopy was acquired using an XPS PHI 5600 (base pressure ∼3 × 10^{-10} Torr) using a monochromatic 15 kV, 300 W Al Kα source ($h\upsilon$ = 1486.6 eV) over a 400 μm spot area. The instrument work function was calibrated to give a binding energy (BE) of 84 eV for the Au $4f_{7/2}$ line for metallic gold, and the spectrometer dispersion was adjusted to give a BE of 932.66 eV for the Cu $2p_{3/2}$ line of metallic copper. An emission angle of 45° and a pass energy of 50 eV were used to acquire high-resolution spectra. A Shirley background was first fitted, following which the component peaks were deconvoluted with pseudo-Voigt line shapes (40:60 Gaussian/Lorentzian) using CasaXPS software. All spectra are referenced to the C 1s aliphatic carbon peak at a binding energy of 284.8 eV.

3. RESULTS AND DISCUSSION

3.1. As-deposited Films. *3.1.1. ALD Process Characterization.* Pulse saturation studies were performed to demonstrate the self-limiting nature of ALD film growth on silicon. Figure 2 shows plots of film growth per cycle (GPC) vs (a) BITSW and (b) H_2S pulse times for 150 cycle films at both T_{DEP} = 315 and 350 °C. For BITSW, a pulse time of 1 s was sufficient to reach a soft saturation at 315 °C, while a 0.8 s pulse was sufficient for hard saturation at 350 °C. For H_2S, a pulse of 0.3 s was needed to achieve hard saturation at 315 °C, while 0.15 s was sufficient for saturation. At 350 °C, the small drop in growth at 0.3 s is within the measurement error of the thickness at the 0.15 and 0.2 s pulses. These results indicate

https://doi.org/10.1021/acs.chemmater.3c00013
Chem. Mater. 2023, 35, 4649−4659

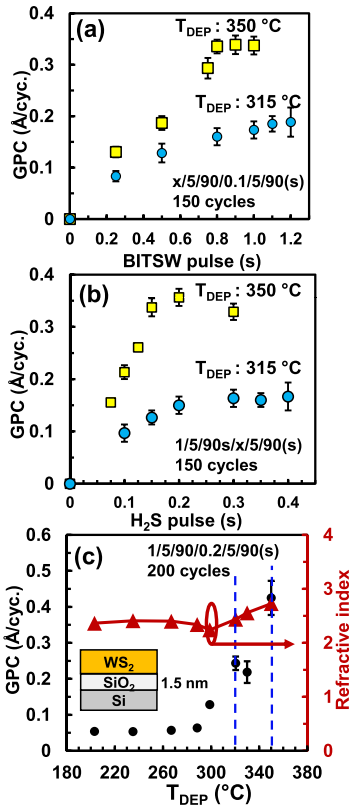

Figure 2. Plots of film GPC vs (a) BITSW and (b) O_2 plasma pulse times for T_{DEP} = 315 (blue circles) and 350 °C (yellow squares) with other pulse times fixed. (c) Plot of GPC (black circles) and refractive index at 1.95 eV (red triangles) vs T_{DEP} for films deposited on silicon. Blue dashed lines indicate the temperature range of saturating growth.

saturating growth between at least T_{DEP} = 315 and 350 °C. Film non-uniformity, calculated as the ratio of standard deviation to the mean film thickness measured over a 5 inch diameter area, was found to increase (from 4 to 10%) for the longer BITSW and H_2S pulse times of 1.2 and 0.4 s (Figure 2a,b). This is likely due to a small CVD component that can arise from leftover excess reactants following a large precursor dose and an insufficient purge.

Shown in Figure 2c is a plot of GPC vs T_{DEP} for 200 cycle films deposited over a temperature range of 200−350 °C. Film growth began at T_{DEP} = 290 °C with little to no growth seen below this temperature. Film GPC generally increased with increasing T_{DEP} up to 350 °C. This was also accompanied by an increase in the film's refractive index from ∼2.4 at 290 °C to 2.9 at 350 °C. These refractive indices are lower than those of bulk 2H-WS_2 (3.8−5).[39] Furthermore, there appears to be a small ALD window of near-constant film growth between 315 and 330 °C. Films deposited above 350 °C showed higher growth and a significant increase in non-uniformity measured over a 5 inch area (∼11%), likely due to the onset of decomposition of BITSW that was reported at this temperature by Mullapudi et al.[35]

3.1.2. Compositional Analysis. An XPS survey scan was performed to examine the elemental composition of films deposited at T_{DEP} = 315 and 350 °C. The survey spectra showed the presence of significant amounts of tungsten, sulfur, and oxygen, along with smaller quantities of silicon and carbon, as well as trace amounts of nitrogen (see Figure S4). Based on these observations, high-resolution scans were then collected for the regions corresponding to the typical range of binding energies for these elements.

Shown in Figure 3 are XPS core-level spectra of tungsten, sulfur, and oxygen for 3.5 and 9 nm thick as-deposited films on

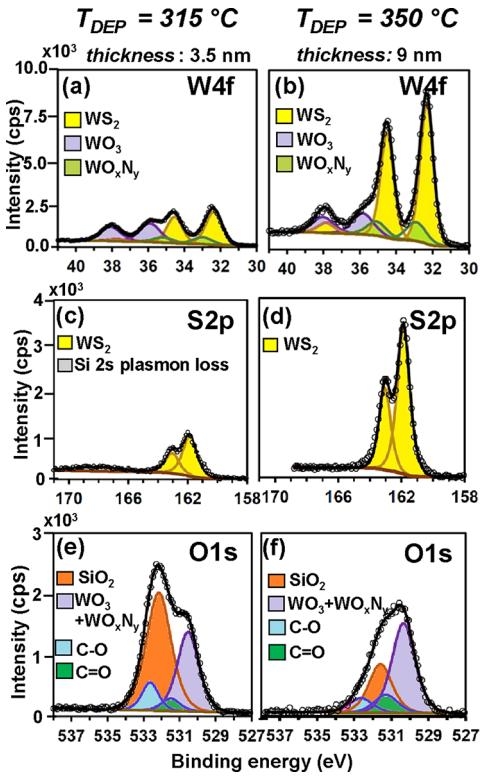

Figure 3. XPS spectra of W 4f, S 2p, and O 1s core levels for ALD films as-deposited at (a,c,e) T_{DEP} = 315 °C (3.5 nm thick) and (b,d,f) T_{DEP} = 350 °C (9 nm thick).

1.5 nm SiO_2/Si substrates using 200 cycles at T_{DEP} = 315 and 350 °C, respectively. For both films, three sets of W $4f_{5/2}$ and W $4f_{7/2}$ doublets, each with a relative peak intensity ratio of 3:4 were fit to the tungsten core levels (Figure 3a,b). The first set of peaks were fit at binding energies of 34.9 and 32.7 eV and arise from WS_2,[3,28,40,41] while a second doublet at 38.4 and 36.2 eV can be attributed to WO_3.[42] To achieve optimal fitting for the signals in this region, a third doublet with binding energies of 35.5 and 33.3 eV was needed. This third doublet, along with an N 1s peak at 397.8 eV (see Figure S5 and Table S1 in Supporting Information), indicates the presence of WO_xN_y in these films.[43] Finally, a small peak at ∼38.1 eV was seen in both films and assigned to the W $5p_{3/2}$ component of WS_2.[44] The intensities of the peaks related to WS_2 and WO_xN_y were found to be higher for films deposited at 350 °C than for those deposited at 315 °C, while the intensities of the WO_3 peaks were found to be similar.

Shown in Figure 3c,d are sulfur core spectra fitted with S $2p_{1/2}$ and S $2p_{3/2}$ doublet peaks at binding energies of 163.4 and 162.2 eV, respectively, with an intensity ratio of 1:2. These peaks, along with the tungsten peaks at 34.8 and 32.7 eV (Figure 3a,b) confirm the presence of WS_2 in both films.[3,28,40] The film deposited at 315 °C showed an additional small broad peak at ∼168.3 eV, likely due to a plasmon loss peak from Si2s detected from the underlying native SiO_2.[44] The percentage composition by chemical state of WS_2 was found to

https://doi.org/10.1021/acs.chemmater.3c00013
Chem. Mater. 2023, 35, 4649−4659

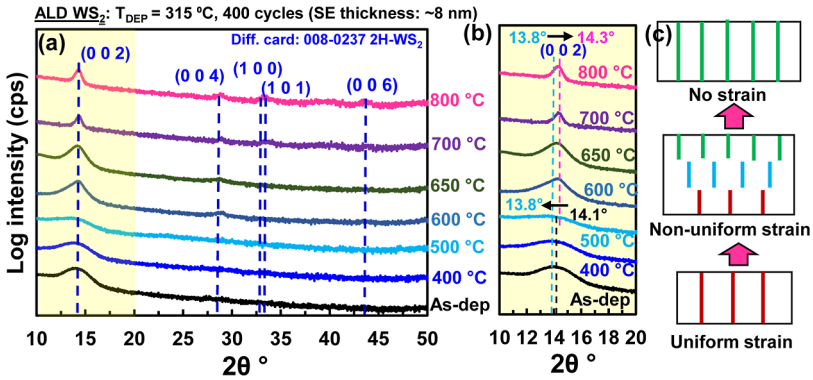

Figure 4. (a) GIXRD scans comparing films as-deposited at T_{DEP} = 315 °C and successive isochronal *ex situ* sulfur anneals; peaks are indicated by blue dashed lines and referenced to the 2H polytype of WS_2 (JCPDS card no: 008-0237); (b) (0 0 2) peak highlighted with shifts and full width at half maximum (FWHM) broadening and subsequent sharpening with sequential anneals; (c) suggested mechanism of lattice strain relaxation causing the effects seen in (b).

be ∼3× higher in the 350 °C film, suggesting a higher WS_2 content at higher deposition temperature (see Table S1).

The core-level scans of oxygen are shown in Figure 3e,f for films deposited at 315 and 350 °C, respectively. The O 1s peak at a binding energy of 530.7 eV along with the tungsten doublet peaks at 36.2 and 38.4 and 35.5 and 33.3 eV (Figure 3a,b) indicate the presence of WO_3 and WO_xN_y in both films. However, further deconvolution of this was not performed given the close proximity of the binding energies of the WO_3 and WO_xN_y components.[43] Additionally, the O 1s peak at ∼532.5 eV along with the Si 2p doublet (Si $2p_{1/2}$ and Si $2p_{3/2}$) at 103.2 and 103.8 eV (see Figure S5 in the Supporting Information) indicate the presence of SiO_2 for films deposited at 315 °C.[45] Films deposited at 350 °C showed the same peaks but at slightly lower binding energies for the O 1s and Si 2p doublets, likely indicating the presence of sub-stoichiometric SiO_x ($x < 2$), the origin of which is discussed below (see Table S1).[46] Finally, small peaks were also seen at binding energies of 531.8 and 532.9 eV, arising from the C−O and C═O groups, respectively, of surface adventitious carbon (see Figure S5 in the Supporting Information).[47]

Other residual impurities such as C and N were also seen at both temperatures (see Figure S5 in the Supporting Information). The C 1s spectra in Figure S5e,f mostly comprising C−C, C−O, and C═O, likely originated from an adventitious layer on the surface of both films. A small portion of the C content exists as C−N. C−N and NH_4 likely originate from *t*-butylimido ligands incorporated or decomposed during chemisorption of BITSW. Finally, the elemental Si peak (see Figure S5c in the Supporting Information) likely originated from the substrate in the thinner (3 nm) T_{DEP} = 315 °C film.

Increasing the deposition temperature from 315 to 350 °C slightly increased the peak area, and thereby, the percentage composition by the chemical state, of WO_xN_y relative to WS_2 (see Figure 3b and Table S1). Previous work by Mullapudi et al. investigating WO_3−SiO_2 films formed via ALD using BITSW and O_2 plasma reported a temperature-dependent competition in chemisorption between the *t*-butylimido and trimethylsilylmethyl ligands of BITSW, in which an increase in chemisorption through the trimethylsilylmethyl ligand was seen at higher temperatures.[35] Following the BITSW pulse, *t*-butylimido ligands that remain after chemisorption can undergo *β*-hydride elimination forming WN as a by-product, which is incorporated in the film, where it can then oxidize to WO_xN_y upon exposure to the environment.[3,48] An increased amount of WO_xN_y (from ∼2 to 5%) seen for films deposited at 350 °C (Figure 3b and Table S1) indicated that more *t*-butylimido groups were left behind at 350 than at 315 °C and therefore implied an increase in chemisorption through the trimethylsilyl ligand at higher deposition temperatures, consistent with earlier work (Figure 3b).[35]

WO_3 appears in both films after exposure to ambient air. This is due to the portion of chemisorbed BITSW that is not converted to WS_2 during the H_2S half-cycle, which can then oxidize to form WO_3 when exposed in the air (Figure 3a,b).[32] The decrease in the peak area of WO_3 relative to that of WS_2 at 350 °C vs 315 °C may therefore be due to the increased reactivity of both ligands with H_2S at higher temperatures.

There are two potential reasons for the SiO_x detected for both films (see Figures 3e,f and S5c,f in the Supporting Information): (i) oxidation of unreacted trimethylsilylmethyl ligands upon exposure to air following deposition, and (ii) the ∼1.5 nm thick native SiO_2 layer from the underlying substrate. Since XPS is surface-sensitive, the SiO_x detected in films deposited at 350 °C can arise entirely due to the former, given that they are ∼9 nm thick.[35] However, for the very thin 3 nm films deposited at 315 °C, at least some of the detected SiO_2 is due to the underlying native oxide, likely accounting for the higher amount of SiO_2 in those films (Figure 3e and Table S1).

3.2. Post-deposition Sulfur Annealing. *3.2.1. XRD.* The crystallinity and grain size of ALD-deposited nanocrystalline films can be improved by using an annealing approach described previously.[49] To understand the evolution of WS_2 crystallites in the 400 cycle films deposited at T_{DEP} = 315 °C, successive 60 min isochronal anneals were performed *ex situ* in an atmosphere of elemental sulfur. Following each successive anneal, the sample was removed from the furnace to perform an *ex situ* GIXRD measurement in the air. Ambient exposure was limited to a maximum of 30 min to minimize the oxidation of the annealed film. Figure 4a shows a comparison of GIXRD scans acquired for the same sample following each successive anneal. As-deposited films were nanocrystalline in nature and showed a broad peak centered at 2θ = 14.1° with a Scherrer estimated crystallite size of 3.7 nm. This peak is close to that of the (0 0 2) 2H polytype of WS_2, normally seen at 14.32° and corresponds to the reflections from the basal planes parallel to the substrate.[23] The slight shift to lower angles is likely due to lattice strain in the film that can develop during deposition (Figure 4c).[50] Upon successive annealing up to 500 °C, the (0

https://doi.org/10.1021/acs.chemmater.3c00013
Chem. Mater. 2023, 35, 4649−4659

0 2) peak was found to broaden slightly and shift to a lower 2θ of 13.8°, shown in further detail in Figure 4b and Table S3 in the Supporting Information. This broadening indicates a decrease in the Scherrer crystallite size to ~2.6 nm at 500 °C. Broadening can occur as a result of non-uniform strain that could arise due to the re-orientation of WS_2 nanocrystalline domains during the annealing process (Figure 4c).[50] Successive anneals at 600 °C and above were found to reverse the lower temperature trend, *sharpening* and shifting the (0 0 2) peak to *larger* 2θ. At 800 °C, the Scherrer crystallite size estimate was ~12.3 nm, and the (0 0 2) peak position of 2θ = 14.3° indicated little to no lattice strain. The impact of increasing the annealing temperature on strain is illustrated schematically in Figure 4c.

Other polycrystalline peaks were also observed for films annealed at 600 °C and above. Reflections of the (0 0 2) basal planes were seen at 2θ = 29.1 and 43.7°, corresponding to the (0 0 4) and (0 0 6) peaks of the 2H WS_2 polytype. Additional reflections at 32.7 and 33.5° were visible for films annealed at 700 and 800 °C and may be attributed to the (1 0 0) and (1 0 1) peaks of 2H WS_2, likely due to growth along directions other than the (0 0 2) basal planes. These peaks were also seen for films as-deposited at T_{DEP} = 350 °C (see Figure S6 in the Supporting Information).[7,22,28]

WO_3 peaks were not detected in any of the scans in Figure 4, taken to indicate an absence of oxidation (as shown in Figure S7, WO_3 peaks were only detected when the furnace developed an atmospheric leak, upon which that experiment was aborted).

3.2.2. Raman Spectra. Shown in Figure 5 are Raman spectra acquired on 400 cycle films (a) as-deposited on silicon

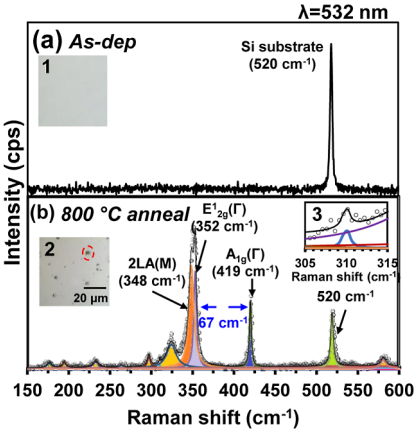

Figure 5. Raman spectra of 400 cycle T_{DEP} = 315 °C films on native SiO_2/Si (a) as-deposited and (b) annealed at 800 °C in elemental sulfur. Insets show optical microscopy images of the film (1) as-deposited and (2) following the anneal; (3) highlight of a vibrational mode at 310 cm^{-1}.

at T_{DEP} = 315 °C and (b) annealed at 800 °C for 1 h in elemental sulfur. Aside from a peak at ~519 cm^{-1} which can be attributed to substrate silicon, no Raman peaks characteristic of those of WS_2 were seen for as-deposited films, even at a higher T_{DEP} of 350 °C. This is likely due to the nanocrystalline nature of the as-deposited films.[30,31,51]

The left inset in Figure 5b shows black crystallites that appear on the surface of the film upon annealing in sulfur at 600 °C and above. These crystallites were a consequence of crystallization of the underlying as-deposited film and will be discussed in the next section. Figure 5b shows a Raman spectrum acquired on these crystallites. Deconvolution of this spectrum indicated the presence of three prominent vibrational modes at shifts of ~349, 353, and 420 cm^{-1}. These modes are characteristic of WS_2 and belong to the longitudinal acoustic phonon (2LA(M)), the in-plane displacement of W and S atoms ($E_{2g}^1(\Gamma)$), and the out-of-plane vibration ($A_{1g}(\Gamma)$), respectively. The 2LA(M) is a second-order mode that originates as a harmonic from the zone edge acoustic phonon (LA(M)) at 176 cm^{-1}, while the latter two are first order Raman modes.[52] The separation between the $E_{2g}^1(\Gamma)$ and $A_{1g}(\Gamma)$ modes was found to be ~67 cm^{-1}, implying the bulk nature of the black WS_2 crystallites. Furthermore, the small FWHM of these modes is indicative of high crystallinity and long-range order (see Table S4 in the Supporting Information).[52,53] Additional second-order Raman modes were seen at 324, 297, 232, 195, and 263 cm^{-1}.[53] These vibrations, along with the 2LA(M) mode, arise due to the resonance of the laser energy (~2.33 eV at 532 nm) with the B exciton in bulk WS_2.[54,55] A vibration at 310 cm^{-1} also indicates multilayered WS_2 and is related to a rigid layer shear mode (right side inset of Figure 5b).[53]

In regions separating these crystallites, no Raman signal was detected (aside from the silicon substrate peak at 519 cm^{-1}, see Figure S8 in the Supporting Information), suggesting that WS_2 was consumed in these areas.

3.2.3. WS_2 Morphology on Silicon. Shown in Figure 6a–c are plan-view SEM images of crystallites following *ex situ* annealing at 800 °C in elemental sulfur of a 400 cycle WS_2 film deposited on silicon at 315 °C. Two types of WS_2 nanostructures were seen: (i) in-plane *flake pyramids* (Figure 6a) and (ii) out-of-plane *flowers* (Figure 6b). Each flake pyramid consists of multiple layers of WS_2 nanosheets with basal planes oriented parallel to the silicon substrate. WS_2 flowers are on average much larger than flake pyramids and comprise multiple layers of WS_2 nanosheets sticking out of the substrate plane along many orientations. Each flower was found to be supported by an underlying network of flake pyramids (Figure 6b,c). Both flower and flake pyramid nanostructures are stoichiometric WS_2 (as measured by EDX analysis, see Figure S9 in the Supporting Information), bulk-like in nature (as previously characterized by their Raman signature, Figure 5b), and evolve in proportions relative to each other after each successive anneal, as will be discussed later.

The schematic in Figure 6d illustrates the primary growth mechanism that we speculate could have been responsible for the above-observed nanostructures. During sulfur annealing, stacking faults and/or irregularities in the as-deposited WS_2 film may give rise to screw dislocation driven (SDD) growth of WS_2 crystallites (see Figure 6d). SDD growth may be assisted by enhanced diffusion/ripening and/or coalescence and may ultimately result in the consumption of the WS_2 film surrounding the crystallite (see inset Figure 6d).[56,57] SSD growth over the duration of the anneal forms multi-layered flake pyramids, with the size of the pyramid likely being dictated by the concentration of the growth medium (deposited WS_2 film and sulfur vapor pressure) surrounding each crystallite.[24,58,59] Additionally, grain boundaries on the flake-pyramids expose reactive edge sites to the sulfur vapor, which may then favor crystallite growth in directions non-parallel to the substrate,[22,34] giving rise to WS_2 flowers, as shown in Figure 6e during the initial stages of formation for a

https://doi.org/10.1021/acs.chemmater.3c00013
Chem. Mater. 2023, 35, 4649–4659

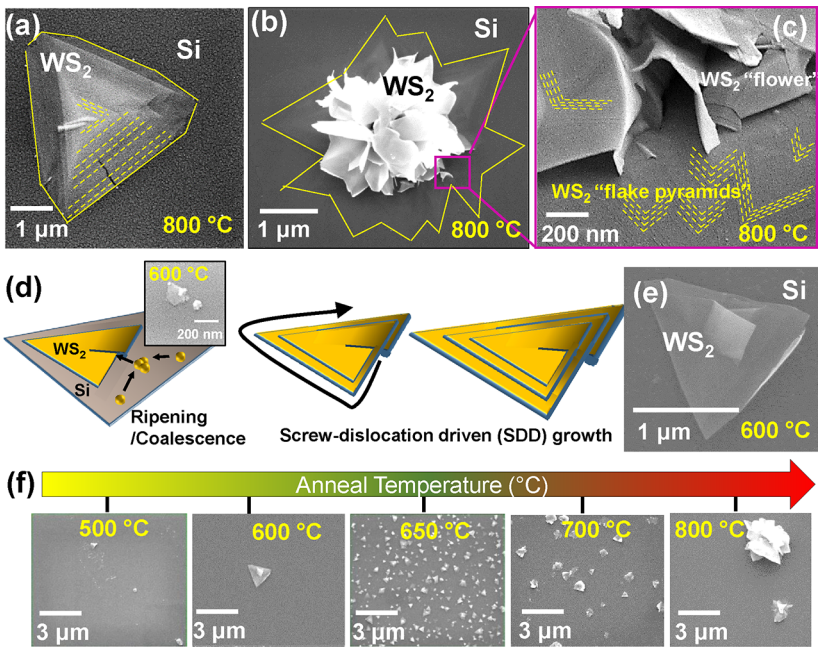

Figure 6. Plan SEM images of (a) multi-layered flake pyramids of WS_2 and (b) WS_2 flowers; (c) network of multi-layered flake pyramids underlying a WS_2 flower in (b) highlighted using yellow dashed-dot lines to guide the eye; (d) schematic illustration of WS_2 crystallite ripening and SDD growth (with an inset SEM image showing the same at 600 °C); (e) SEM image of an out-of-plane growth event on a multi-layered flake pyramid, marking the beginning of a 3-D flower; (f) SEM images showing the evolution of WS_2 crystallite morphology, following sequential anneals at increasing temperature.

film annealed at 600 °C. The presence of both flake pyramids and flowers on the same substrate might be attributed to the local variations in sulfur vapor concentrations expected due to gas flow variations in the crude tube furnace anneals.[24,59]

For WS_2 films deposited and annealed on silicon, the total number of crystallites (both flake pyramids and flowers) seen via SEM generally increased upon increasing the annealing temperature. No crystallite formation was seen for films annealed at 500 °C. Film crystallinity improved for films annealed at 600 °C and above, where crystallites as large as 1 μm (distinct from the Scherrer estimate of perpendicular-to-plane crystallite size discussed previously in section 3.2.1. above)could be found (Figure 6e). This is the largest reported crystallite size to date for ALD WS_2 (see Figure 1), even though they were sparsely distributed. Crystallite growth is further evidenced by a sharpening of FWHM of 2H WS_2 (0 0 2) peak at 600 °C (see Figure 4b and Table S3 in the Supporting Information). A subsequent anneal at 650 °C significantly increased the number of WS_2 crystallites, with ~2000 crystallites observed over a 25 × 25 μm^2 field area, with sizes ranging from less than 100 nm up to around two microns (see Figure S10 in the Supporting Information). However, the average in-plane crystallite size measured using SEM was still much less than a micron. Subsequent anneals at 700 and 800 °C significantly increased the in-plane crystallite size beyond 1 μm, with crystallites up to 3 μm seen at 800 °C. This was also accompanied by an increase in Scherrer crystallite size further beyond 10 nm (see Table S3 in Supporting Information) and may be attributed to either an improved overall film crystallinity and/or an increase in thickness of WS_2 crystallites (perpendicular to (0 0 2) plane). The predominant appearance of micron-sized flower nanostructures seen via SEM, along with a decrease in the average number of crystallites observed over the unit area, implies that the increase in Scherrer crystallite size may be due to the latter and is assisted by enhanced diffusion/crystal ripening.

Not only the concentrations but also the relative proportion of WS_2 flake pyramids to flowers were found to depend on the annealing temperature. While too few crystallites were seen at 600 °C to assess the preference of one nanostructure morphology over the other, films annealed at 650 °C showed a preference for flake pyramids over flowers (see Figure 6f). Subsequent annealing at 700 °C increased the preference for out-of-plane growth so that more flowers grew on top of the existing pyramids, while films annealed at 800 °C showed further preference for out-of-plane growth, resulting in numerous flowers. A similar influence of growth temperature over morphology was reported for MoS_2 and WS_2 films by Li et al., who observed a transition from fullerene-like nano-flowers at 650 °C to nanotubes at 750 °C.[23]

3.2.4. WS_2 Nanostructures on ZnS and Al_2O_3. WS_2 crystallite morphology was also found to be dependent on the underlying substrate on which the film was deposited. Shown in Figure 7 are WS_2 nanostructures formed following post-deposition elemental sulfur annealing of 200 cycle WS_2 films deposited at 315 °C on 4.5 nm ALD ZnS on Si and 30 nm ALD Al_2O_3 on Si. For films deposited at 315 °C, film thickness on ZnS was ~11 nm, while little to no film growth was apparent on Al_2O_3 (see Figure S11 in the Supporting Information).

Annealing at 800 °C of films deposited on ZnS (shown in Figure 7a,b) resulted in only WS_2 flower growth, with little to no flake pyramid growth seen. Moreover, the morphology of flowers grown on ZnS was "crumpled" in nature and differed from that of flowers grown on silicon in that there were no networks of multi-layer flake pyramids found underneath any of the flowers. This may be due to a change in primary growth mechanism from SDD to flower-like growth, with the

https://doi.org/10.1021/acs.chemmater.3c00013
Chem. Mater. 2023, 35, 4649−4659

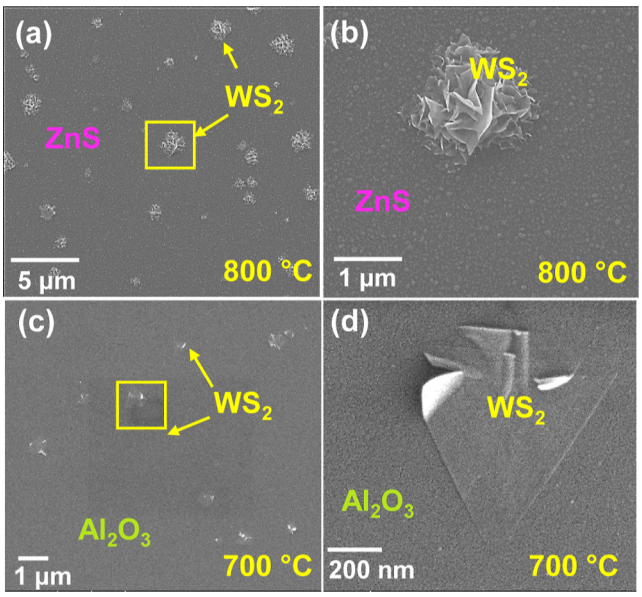

Figure 7. Plan SEM images of WS_2 nanostructures following post-sulfur annealing of 200 cycle films deposited at 315 °C on either (a) 4.5 nm ZnS/Si or (c) 30 nm Al_2O_3/Si; (b,d) higher-magnification SEM images correspond to the areas highlighted by a yellow box in (a,c).

underlying ZnS not only influencing the growth orientation but also potentially acting as an additional source of sulfur during the anneal to effectively increase the local concentration of precursors.[58−60] These structures have a high density of WS_2 edge sites and may be suitable for catalysis.

In contrast, 700 °C annealing of films grown on Al_2O_3 substrates (shown in Figure 7c,d) resulted in mostly in-plane WS_2 flakes of only a few monolayers thick. While the exact reason for this preference is unknown, we believe that sparse island nucleation of the as-deposited film limited the available growth medium concentration and hence favored the lateral, in-plane mode of growth. More work is required to confirm. If the growth on Al_2O_3 can be better controlled to control nucleation and promote lateral growth, the few-layered nature of these structures may be very suitable for device fabrication.

4. SUMMARY AND CONCLUSIONS

A new thermal ALD process to deposit WS_2 was demonstrated using a novel tungsten precursor bis(*t*-butylimido)bis-(trimethylsilylmethyl)tungsten and H_2S. Film growth (measured using SE) on silicon was observed at 290 °C and above with self-limiting growth behavior seen between 315 and 350 °C. As-deposited films were nanocrystalline but did not show characteristic Raman modes for WS_2. Elemental analysis using XPS indicated the presence of WO_3 and WS_2 along with small amounts of WO_xN_y and SiO_x. As the deposition temperature was increased from 315 to 350 °C, the optical refractive index increased from 2.5 to 2.8.

Post-deposition annealing at 600 °C and above in elemental sulfur improved crystallization and WS_2 stoichiometry and potentially converted WO_3 to WS_2.[16,26] GIXRD showed peaks aligned to the 2H WS_2 polytype with crystallite sizes up to 1.5 μm, the largest reported to date for ALD. For films annealed at 800 °C, Raman revealed the emergence of the 2LA(M), $E_{2g}^1(\Gamma)$, and $A_{1g}(\Gamma)$ modes for WS_2. The underlying substrate was found to impact crystallite morphology. Two morphologies of WS_2 crystallites are observed for films annealed on silicon: multilayered (i) flake pyramids (with basal planes parallel to the substrate) and (ii) flowers (resulting from out-of-plane growth from the tops of underlying flake pyramids), with the former dominating up to 650 °C and the latter between 700 and 800 °C. Films deposited and annealed on 4.5 nm ZnS/Si were found to crystallize into micron-sized "crumpled" WS_2 flowers (with no underlying pyramids) with a high density of edge sites. Finally, films deposited and annealed on 30 nm Al_2O_3/Si crystallized into few-layered in-plane WS_2 flakes up to 800 nm across.

This work further shows that the approach of annealing ALD-deposited 2D TMD films holds promise for improving crystallinity and grain size.[49] Further investigation is needed to improve control over crystallite size, morphology, and the number of layers through optimization of deposition temperature, initial film thickness, underlying substrates, nucleation density, and sulfur flux during annealing. With optimization of these parameters, the growth of large, few-layer, in-plane 2D WS_2 flakes produced on Al_2O_3 substrates may be improved toward monolayer control and may find application in high-performance FETs, while the 3D flowers with high edge-site density found on Si and ZnS should be useful for enhanced HER catalysis.

■ ASSOCIATED CONTENT

Supporting Information

The Supporting Information is available free of charge at https://pubs.acs.org/doi/10.1021/acs.chemmater.3c00013.

Physical properties of BITSW; elemental sulfur annealing setup and process; comparison of thickness extracted using Cauchy and Tauc−Lorentz oscillator model; XPS survey spectra for films as-deposited at T_{DEP} = 315 and 350 °C; tabulated values of XPS bond percentages; table of positions of XPS spin−orbit components; XPS spectra of N 1s, Si 2p and C 1s for films as-deposited; Tabulated values of (0 0 2) peak FWHM and respective Scherrer crystallite sizes, GIXRD scans of films as-deposited at various T_{DEP}; GIXRD scan of an aborted anneal experiment upon film oxidation; Raman line scans of optical observed crystallites and their surrounding areas; tabulated positions and FWHM of various Raman component peaks for WS_2 crystallites; EDX spectra acquired for a WS_2 flower and its respective atomic % and weight % values; crystallite size distribution for a 400 cycle, T_{DEP} = 315 °C film deposited on silicon and successively annealed until 650 °C; and thickness vs T_{DEP} for WS_2 films deposited on 30 nm ALD Al_2O_3 (PDF)

■ AUTHOR INFORMATION

Corresponding Author

John. F. Conley, Jr. − *School of Electrical Engineering and Computer Science, Oregon State University, Corvallis, Oregon 97331, United States;* orcid.org/0000-0001-7407-9290; Email: jconley@eecs.oregonstate.edu

Authors

Kamesh Mullapudi − *School of Electrical Engineering and Computer Science, Oregon State University, Corvallis, Oregon 97331, United States;* Present Address: ASM America,

https://doi.org/10.1021/acs.chemmater.3c00013
Chem. Mater. 2023, 35, 4649−4659

3440 E University Dr, Phoenix, AZ 85034, United States; orcid.org/0000-0002-1731-6808

Rafik Addou − *School of Chemical, Biological, and Environmental Engineering, Oregon State University, Corvallis, Oregon 97331, United States;* orcid.org/0000-0002-5454-0315

Charles. L. Dezelah − *EMD Electronics, Haverhill, Massachusetts 01832, United States;* Present Address: ASM Microchemistry Oy, Pietari Kalmin katu 3, F 2, Helsinki, Finland 00560.

Daniel F. Moser − *EMD Electronics, Haverhill, Massachusetts 01832, United States*

Ravindra K. Kanjolia − *EMD Electronics, Haverhill, Massachusetts 01832, United States*

Jacob H. Woodruff − *EMD Electronics, Haverhill, Massachusetts 01832, United States*

Complete contact information is available at: https://pubs.acs.org/10.1021/acs.chemmater.3c00013

Notes

The authors declare no competing financial interest.

■ ACKNOWLEDGMENTS

The authors thank EMD Performance Materials (now EMD Electronics) for the partial funding of this work and for providing the tungsten precursor (BITSW) and Chris Tasker (MaSC, OSU) for his assistance in the modification of the ALD reactor for improved precursor delivery. This work was conducted at the OSU Materials Synthesis and Characterization (MaSC) user Facility at the Northwest Nanotechnology Infrastructure (NNI), a National Nanotechnology Coordinated Infrastructure (NNCI) site at the Oregon State University, which is supported in part by the National Science Foundation (grant NNCI-1542101).

■ REFERENCES

(1) Sarma, P. V.; Vineesh, T. V.; Kumar, R.; Sreepal, V.; Prasannachandran, R.; Singh, A. K.; Shaijumon, M. M. Nanostructured Tungsten Oxysulfide as an Efficient Electrocatalyst for Hydrogen Evolution Reaction. *ACS Catal.* **2020**, *10*, 6753−6762.

(2) Lee, N.; Kwak, J.; Kwak, J. H.; Jung, S.-M.; Kim, J.; Giri, A.; Thiyagarajan, K.; Kim, Y.-T.; Jung, S.; Kim, J. K.; Jeong, U. Microwave-Assisted Evolution of WO_3 and WS_2/WO_3 Hierarchical Nanotrees. *J. Mater. Chem. A* **2020**, *8*, 9654−9660.

(3) Kim, D.-H.; Ramesh, R.; Nandi, D. K.; Bae, J.-S.; Kim, S.-H. Atomic Layer Deposition of Tungsten Sulfide Using a New Metal-Organic Precursor and H_2S: Thin Film Catalyst for Water Splitting. *Nanotechnology* **2020**, *32*, 075405.

(4) Balasubramanyam, S.; Shirazi, M.; Bloodgood, M. A.; Wu, L.; Verheijen, M. A.; Vandalon, V.; Kessels, W. M. M.; Hofmann, J. P.; Bol, A. A. Edge-Site Nanoengineering of WS_2 by Low-Temperature Plasma-Enhanced Atomic Layer Deposition for Electrocatalytic Hydrogen Evolution. *Chem. Mater.* **2019**, *31*, 5104−5115.

(5) Sarma, P. V.; Kayal, A.; Sharma, C. H.; Thalakulam, M.; Mitra, J.; Shaijumon, M. M. Electrocatalysis on Edge-Rich Spiral WS_2 for Hydrogen Evolution. *ACS Nano* **2019**, *13*, 10448−10455.

(6) Scharf, T. W.; Prasad, S. V.; Mayer, T. M.; Goeke, R. S.; Dugger, M. T. Atomic Layer Deposition of Tungsten Disulphide Solid Lubricant Thin Films. *J. Mater. Res.* **2004**, *19*, 3443−3446.

(7) Scharf, T. W.; Prasad, S. V.; Dugger, M. T.; Kotula, P. G.; Goeke, R. S.; Grubbs, R. K. Growth, Structure, and Tribological Behavior of Atomic Layer-Deposited Tungsten Disulphide Solid Lubricant Coatings with Applications to MEMS. *Acta Mater.* **2006**, *54*, 4731−4743.

(8) Nandi, D. K.; Sen, U. K.; Dhara, A.; Mitra, S.; Sarkar, S. K. Intercalation Based Tungsten Disulfide (WS_2) Li-Ion Battery Anode Grown by Atomic Layer Deposition. *RSC Adv.* **2016**, *6*, 38024−38032.

(9) Yeo, S.; Nandi, D. K.; Rahul, R.; Kim, T. H.; Shong, B.; Jang, Y.; Bae, J.-S.; Han, J. W.; Kim, S.-H.; Kim, H. Low-Temperature Direct Synthesis of High Quality WS_2 Thin Films by Plasma-Enhanced Atomic Layer Deposition for Energy Related Applications. *Appl. Surf. Sci.* **2018**, *459*, 596−605.

(10) Nandi, D. K.; Yeo, S.; Ansari, M. Z.; Sinha, S.; Cheon, T.; Kwon, J.; Kim, H.; Heo, J.; Song, T.; Kim, S.-H. Thickness-Dependent Electrochemical Response of Plasma Enhanced Atomic Layer Deposited WS_2 Anodes in Na-Ion Battery. *Electrochim. Acta* **2019**, *322*, 134766.

(11) Wang, Q.; Zhang, Q.; Luo, X.; Wang, J.; Zhu, R.; Liang, Q.; Zhang, L.; Yong, J. Z.; Yu Wong, C. P.; Eda, G.; Smet, J. H.; Wee, A. T. S. Optoelectronic Properties of a van Der Waals WS_2 Monolayer/2D Perovskite Vertical Heterostructure. *ACS Appl. Mater. Interfaces* **2020**, *12*, 45235−45242.

(12) Wu, F.; Tian, H.; Shen, Y.; Hou, Z.; Ren, J.; Gou, G.; Sun, Y.; Yang, Y.; Ren, T.-L. Vertical MoS_2 Transistors with Sub-1-Nm Gate Lengths. *Nature* **2022**, *603*, 259−264.

(13) Sebastian, A.; Pendurthi, R.; Choudhury, T. H.; Redwing, J. M.; Das, S. Benchmarking Monolayer MoS_2 and WS_2 Field-Effect Transistors. *Nat. Commun.* **2021**, *12*, 693.

(14) Liu, L.; Kumar, S. B.; Ouyang, Y.; Guo, J. Performance Limits of Monolayer Transition Metal Dichalcogenide Transistors. *IEEE Trans. Electron Devices* **2011**, *58*, 3042−3047.

(15) Georgiou, T.; Jalil, R.; Belle, B. D.; Britnell, L.; Gorbachev, R. V.; Morozov, S. V.; Kim, Y.-J.; Gholinia, A.; Haigh, S. J.; Makarovsky, O.; Eaves, L.; Ponomarenko, L. A.; Geim, A. K.; Novoselov, K. S.; Mishchenko, A. Vertical Field-Effect Transistor Based on Graphene−WS_2 Heterostructures for Flexible and Transparent Electronics. *Nat. Nanotechnol.* **2013**, *8*, 100−103.

(16) Song, J.-G.; Park, J.; Lee, W.; Choi, T.; Jung, H.; Lee, C. W.; Hwang, S.-H.; Myoung, J. M.; Jung, J.-H.; Kim, S.-H.; Lansalot-Matras, C.; Kim, H. Layer-Controlled, Wafer-Scale, and Conformal Synthesis of Tungsten Disulfide Nanosheets Using Atomic Layer Deposition. *ACS Nano* **2013**, *7*, 11333−11340.

(17) Chubarov, M.; Choudhury, T. H.; Hickey, D. R.; Bachu, S.; Zhang, T.; Sebastian, A.; Bansal, A.; Zhu, H.; Trainor, N.; Das, S.; Terrones, M.; Alem, N.; Redwing, J. M. Wafer-Scale Epitaxial Growth of Unidirectional WS_2 Monolayers on Sapphire. *ACS Nano* **2021**, *15*, 2532−2541.

(18) Groven, B.; Nalin Mehta, A.; Bender, H.; Meersschaut, J.; Nuytten, T.; Verdonck, P.; Conard, T.; Smets, Q.; Schram, T.; Schoenaers, B.; Stesmans, A.; Afanas'ev, V.; Vandervorst, W.; Heyns, M.; Caymax, M.; Radu, I.; Delabie, A. Two-Dimensional Crystal Grain Size Tuning in WS Atomic Layer Deposition: An Insight in the Nucleation Mechanism. *Chem. Mater.* **2018**, *30*, 7648−7663.

(19) Browning, R.; Plachinda, P.; Padigi, P.; Solanki, R.; Rouvimov, S. Growth of Multiple WS_2/SnS Layered Semiconductor Heterojunctions. *Nanoscale* **2016**, *8*, 2143−2148.

(20) Yang, H.; Wang, Y.; Zou, X.; Bai, R.-X.; Han, S.; Wu, Z.; Han, Q.; Zhang, Y.; Zhu, H.; Chen, L.; Lu, X.; Sun, Q.; Lee, J. C.; Yu, E. T.; Akinwande, D.; Ji, L. Growth Mechanisms and Morphology Engineering of Atomic Layer-Deposited WS_2. *ACS Appl. Mater. Interfaces* **2021**, *13*, 43115−43122.

(21) Yang, H.; Wang, Y.; Zou, X.; Bai, R.; Wu, Z.; Han, S.; Chen, T.; Hu, S.; Zhu, H.; Chen, L.; Zhang, D. W.; Lee, J. C.; Lu, X.; Zhou, P.; Sun, Q.; Yu, E. T.; Akinwande, D.; Ji, L. Wafer-Scale Synthesis of WS_2 Films with In Situ Controllable p-Type Doping by Atomic Layer Deposition. *Research* **2021**, *2021*, DOI: 10.34133/2021/9862483.

(22) Chung, J.-W.; Dai, Z. R.; Ohuchi, F. S. WS_2 Thin Films by Metal Organic Chemical Vapor Deposition. *J. Cryst. Growth* **1998**, *186*, 137−150.

(23) Li, X.-L.; Ge, J.-P.; Li, Y.-D. Atmospheric Pressure Chemical Vapor Deposition: An Alternative Route to Large-Scale MoS_2 and

WS_2 Inorganic Fullerene-like Nanostructures and Nanoflowers. *Chem.—Eur J.* **2004**, *10*, 6163−6171.
(24) Sarma, P. V.; Patil, P. D.; Barman, P. K.; Kini, R. N.; Shaijumon, M. M. Controllable Growth of Few-Layer Spiral WS_2. *RSC Adv.* **2016**, *6*, 376−382.
(25) Cao, S.; Liu, T.; Zeng, W.; Hussain, S.; Peng, X.; Pan, F. Synthesis and Characterization of Flower-like WS_2 Nanospheres via a Facile Hydrothermal Route. *J. Mater. Sci.: Mater. Electron.* **2014**, *25*, 4300−4305.
(26) Thangaraja, A.; Shinde, S. M.; Kalita, G.; Tanemura, M. Effect of WO_3 Precursor and Sulfurization Process on WS_2 Crystals Growth by Atmospheric Pressure CVD. *Mater. Lett.* **2015**, *156*, 156−160.
(27) Romanov, R. I.; Kozodaev, M. G.; Chernikova, A. G.; Zabrosaev, I. V.; Chouprik, A. A.; Zarubin, S. S.; Novikov, S. M.; Volkov, V. S.; Markeev, A. M. Thickness-Dependent Structural and Electrical Properties of WS2 Nanosheets Obtained via the ALD-Grown WO3 Sulfurization Technique as a Channel Material for Field-Effect Transistors. *ACS Omega* **2021**, *6*, 34429−34437.
(28) Delabie, A.; Caymax, M.; Groven, B.; Heyne, M.; Haesevoets, K.; Meersschaut, J.; Nuytten, T.; Bender, H.; Conard, T.; Verdonck, P.; Van Elshocht, S.; De Gendt, S.; Heyns, M.; Barla, K.; Radu, I.; Thean, A. Low Temperature Deposition of 2D WS_2 Layers from WF_6 and H_2S Precursors: Impact of Reducing Agents. *Chem. Commun.* **2015**, *51*, 15692−15695.
(29) Groven, B.; Heyne, M.; Nalin Mehta, A.; Bender, H.; Nuytten, T.; Meersschaut, J.; Conard, T.; Verdonck, P.; Van Elshocht, S.; Vandervorst, W.; De Gendt, S.; Heyns, M.; Radu, I.; Caymax, M.; Delabie, A. Plasma-Enhanced Atomic Layer Deposition of Two-Dimensional WS_2 from WF_6, H_2 Plasma, and H_2S. *Chem. Mater.* **2017**, *29*, 2927−2938.
(30) Groven, B.; Tomczak, Y.; Heyns, M.; Radu, I.; Delabie, A. Two-Dimensional WS_2 Crystals at Predetermined Locations by Anisotropic Growth during Atomic Layer Deposition. *J. Appl. Phys.* **2020**, *128*, 175302.
(31) Mattinen, M.; Hatanpää, T.; King, P. J.; Meinander, K.; Mizohata, K.; Jalkanen, P.; Räisänen, J.; Ritala, M.; Leskelä, M. Crystalline Tungsten Sulfide Thin Films by Atomic Layer Deposition and Mild Annealing. *J. Vac. Sci. Technol., A* **2019**, *37*, 020921.
(32) Wu, Y.; Raza, M. H.; Chen, Y.-C.; Amsalem, P.; Wahl, S.; Skrodczky, K.; Xu, X.; Lokare, K. S.; Zhukush, M.; Gaval, P.; Koch, N.; Quadrelli, E. A.; Pinna, N. A Self-Limited Atomic Layer Deposition of WS_2 Based on the Chemisorption and Reduction of Bis(t-Butylimino)Bis(Dimethylamino) Complexes. *Chem. Mater.* **2019**, *31*, 1881−1890.
(33) Ikeda, Y.; Ueno, K. Low-Temperature Growth of Crystalline Tungsten Disulfide Thin Films by Using Organic Liquid Precursors. *Jpn. J. Appl. Phys.* **2019**, *59*, SCCC04.
(34) Balasubramanyam, S.; Bloodgood, M. A.; van Ommeren, M.; Faraz, T.; Vandalon, V.; Kessels, W. M. M.; Verheijen, M. A.; Bol, A. A. Probing the Origin and Suppression of Vertically Oriented Nanostructures of 2D WS_2 Layers. *ACS Appl. Mater. Interfaces* **2020**, *12*, 3873−3885.
(35) Mullapudi, K.; Holden, K. E. K.; Peterson, J. L.; Dezelah, C. L.; Moser, D. F.; Kanjolia, R. K.; Tweet, D. J.; Conley, J. F., Jr. Plasma-Enhanced Atomic Layer Deposition of WO_3-SiO_2 Films Using a Heteronuclear Precursor. *J. Vac. Sci. Technol., A* **2023**, *41*, 012406.
(36) Valdivia, A.; Tweet, D. J.; Conley, J. F., Jr. Atomic Layer Deposition of Two Dimensional MoS_2 on 150 mm Substrates. *J. Vac. Sci. Technol., A* **2016**, *34*, 021515.
(37) Balasubramanyam, S.; Merkx, M. J. M.; Verheijen, M. A.; Kessels, W. M. M.; Mackus, A. J. M.; Bol, A. A. Area-Selective Atomic Layer Deposition of Two-Dimensional WS2 Nanolayers. *ACS Mater. Lett.* **2020**, *2*, 511−518.
(38) Atkin, P.; Lau, D. W. M.; Zhang, Q.; Zheng, C.; Berean, K. J.; Field, M. R.; Ou, J. Z.; Cole, I. S.; Daeneke, T.; Kalantar-Zadeh, K. Laser Exposure Induced Alteration of WS_2 Monolayers in the Presence of Ambient Moisture. *2D Mater.* **2017**, *5*, 015013.
(39) Ballif, C.; Regula, M.; Lévy, F. Optical and Electrical Properties of Semiconducting WS_2 Thin Films: From Macroscopic to Local Probe Measurements. *Sol. Energy Mater. Sol. Cells* **1999**, *57*, 189−207.
(40) Xie, X.; McCarley, R. E. Synthesis, Structure, and Characterization of N-Ligated Tungsten Selenide Cluster Complexes $W_6Se_8L_6$. *Inorg. Chem.* **1995**, *34*, 6124−6129.
(41) Morgan, D. J. Core-level spectra of powdered tungsten disulfide, WS2. *Surf. Sci. Spectra* **2018**, *25*, 014002.
(42) Gassman, P. G.; Macomber, D. W.; Willging, S. M. Isolation and Characterization of Reactive Intermediates and Active Catalysts in Homogeneous Catalysis. *J. Am. Chem. Soc.* **1985**, *107*, 2380−2388.
(43) Zhao, Y. M.; Hu, W. B.; Xia, Y. D.; Smith, E. F.; Zhu, Y. Q.; Dunnill, C. W.; Gregory, D. H. Preparation and Characterization of Tungsten Oxynitride Nanowires. *J. Mater. Chem.* **2007**, *17*, 4436−4440.
(44) Moulder, J. F. *Handbook of X-Ray Photoelectron Spectroscopy: A Reference Book of Standard Spectra for Identification and Interpretation of XPS Data*; Physical Electronics Division, Perkin-Elmer Corporation, 1992.
(45) Gross, Th.; Ramm, M.; Sonntag, H.; Unger, W.; Weijers, H. M.; Adem, E. H. An XPS Analysis of Different SiO2 Modifications Employing a C 1s as Well as an Au 4f7/2 Static Charge Reference. *Surf. Interface Anal.* **1992**, *18*, 59−64.
(46) Alfonsetti, R.; De Simone, G.; Lozzi, L.; Passacantando, M.; Picozzi, P.; Santucci, S. SiOx Surface Stoichiometry by XPS: A Comparison of Various Methods. *Surf. Interface Anal.* **1994**, *22*, 89−92.
(47) Swift, P. Adventitious Carbon—the Panacea for Energy Referencing? *Surf. Interface Anal.* **1982**, *4*, 47−51.
(48) Becker, J. S.; Suh, S.; Wang, S.; Gordon, R. G. Highly Conformal Thin Films of Tungsten Nitride Prepared by Atomic Layer Deposition from a Novel Precursor. *Chem. Mater.* **2003**, *15*, 2969−2976.
(49) Mattinen, M.; Leskelä, M.; Ritala, M. Atomic Layer Deposition of 2D Metal Dichalcogenides for Electronics, Catalysis, Energy Storage, and Beyond. *Adv. Mater. Interfac.* **2021**, *8*, 2001677.
(50) Cullity, B. D.; Stock, S. R. *Elements of X-Ray Diffraction*, 3rd ed.; Prentice-Hall: New York, 2001.
(51) Mattinen, M.; Gity, F.; Coleman, E.; Vonk, J. F. A.; Verheijen, M. A.; Duffy, R.; Kessels, W. M. M.; Bol, A. A. Atomic Layer Deposition of Large-Area Polycrystalline Transition Metal Dichalcogenides from 100 °C through Control of Plasma Chemistry. *Chem. Mater.* **2022**, *34*, 7280−7292.
(52) Berkdemir, A.; Gutiérrez, H. R.; Botello-Méndez, A. R.; Perea-López, N.; Elías, A. L.; Chia, C.-I.; Wang, B.; Crespi, V. H.; López-Urías, F.; Charlier, J.-C.; Terrones, H.; Terrones, M. Identification of Individual and Few Layers of WS_2 Using Raman Spectroscopy. *Sci. Rep.* **2013**, *3*, 1755.
(53) Zhao, W.; Ghorannevis, Z.; Amara, K. K.; Pang, J. R.; Toh, M.; Zhang, X.; Kloc, C.; Tan, P. H.; Eda, G. Lattice Dynamics in Mono- and Few-Layer Sheets of WS_2 and WSe_2. *Nanoscale* **2013**, *5*, 9677−9683.
(54) Zhang, X.; Qiao, X.-F.; Shi, W.; Wu, J.-B.; Jiang, D.-S.; Tan, P.-H. Phonon and Raman Scattering of Two-Dimensional Transition Metal Dichalcogenides from Monolayer, Multilayer to Bulk Material. *Chem. Soc. Rev.* **2015**, *44*, 2757−2785.
(55) Mitioglu, A. A.; Plochocka, P.; Deligeorgis, G.; Anghel, S.; Kulyuk, L.; Maude, D. K. Second-Order Resonant Raman Scattering in Single-Layer Tungsten Disulfide WS_2. *Phys. Rev. B: Condens. Matter Mater. Phys.* **2014**, *89*, 245442.
(56) Ouyang, R.; Liu, J.-X.; Li, W.-X. Atomistic Theory of Ostwald Ripening and Disintegration of Supported Metal Particles under Reaction Conditions. *J. Am. Chem. Soc.* **2013**, *135*, 1760−1771.
(57) Grillo, F.; Van Bui, H.; Moulijn, J. A.; Kreutzer, M. T.; van Ommen, J. R. Understanding and Controlling the Aggregative Growth of Platinum Nanoparticles in Atomic Layer Deposition: An Avenue to Size Selection. *J. Phys. Chem. Lett.* **2017**, *8*, 975−983.
(58) Markov, I. V. *Crystal Growth for Beginners: Fundamentals of Nucleation, Crystal Growth and Epitaxy*; World Scientific, 1995.

https://doi.org/10.1021/acs.chemmater.3c00013
Chem. Mater. 2023, 35, 4649−4659

(59) Chen, L.; Liu, B.; Abbas, A. N.; Ma, Y.; Fang, X.; Liu, Y.; Zhou, C. Screw-Dislocation-Driven Growth of Two-Dimensional Few-Layer and Pyramid-like WSe_2 by Sulfur-Assisted Chemical Vapor Deposition. *ACS Nano* **2014**, *8*, 11543−11551.
(60) Zhao, Y.; Jin, S. Stacking and Twisting of Layered Materials Enabled by Screw Dislocations and Non-Euclidean Surfaces. *Acc. Mater. Res.* **2022**, *3*, 369−378.

https://doi.org/10.1021/acs.chemmater.3c00013
Chem. Mater. 2023, 35, 4649−4659